JGR Solid Earth

RESEARCH ARTICLE
10.1029/2022JB025279

Earthquake Detection Using a Nodal Array on the San Jacinto Fault in California: Evidence for High Foreshock Rates Preceding Many Events

Peter M. Shearer[1], Haoran Meng[1,2], and Wenyuan Fan[1]

[1]Scripps Institution of Oceanography, UC San Diego, La Jolla, CA, USA, [2]Department of Earth and Space Sciences, Southern University of Science and Technology, Shenzhen, Guangdong, China

Key Points:

- We detect over 13,000 seismic events during 26 days in 2014 using a dense nodal array on the San Jacinto fault zone in southern California
- Most of the detections are newly discovered earthquakes not in existing catalogs
- Foreshocks are common among these earthquakes, increasing in the rate before their mainshocks following an inverse Omori's law

Supporting Information:

Supporting Information may be found in the online version of this article.

Correspondence to:

P. M. Shearer,
pshearer@ucsd.edu

Citation:

Shearer, P. M., Meng, H., & Fan, W. (2023). Earthquake detection using a nodal array on the San Jacinto fault in California: Evidence for high foreshock rates preceding many events. *Journal of Geophysical Research: Solid Earth*, *128*, e2022JB025279. https://doi.org/10.1029/2022JB025279

Received 27 JUL 2022
Accepted 16 NOV 2022

Author Contributions:

Conceptualization: Peter M. Shearer, Haoran Meng, Wenyuan Fan
Funding acquisition: Peter M. Shearer, Wenyuan Fan
Methodology: Peter M. Shearer, Haoran Meng, Wenyuan Fan
Software: Peter M. Shearer, Haoran Meng, Wenyuan Fan
Supervision: Peter M. Shearer, Wenyuan Fan
Writing – original draft: Haoran Meng
Writing – review & editing: Peter M. Shearer, Wenyuan Fan

Abstract We use a dense seismic array of 1,108 vertical-component geophones within a 600-m footprint to detect thousands of small earthquakes near an active strand of the San Jacinto fault zone in southern California during a 26-day period. We first correct site effects using multichannel cross-correlations of the P-waves of 256 cataloged earthquakes, and then perform beamforming analysis on the continuous waveforms in a slowness range from −0.4 to 0.4 s/km in both the east and north directions. At each time step, we identify the beam slowness with maximum amplitude and apply a picking algorithm to identify 13,408 events. These detections include over 55.6% of the events in the Quake Template Matching (QTM) catalog for all of southern California during the same time period and 70% of those within 100 km of the array. In addition, we detect over 10,000 new events, not in the QTM catalog. Many of these events can also be seen in records from nearby borehole seismic stations. Measured slownesses for the catalog and newly-discovered events group into clusters that can be associated with QTM earthquake locations, but with slowness values considerably distorted from predictions based on a 1-D velocity model, presumably owing to strong velocity heterogeneity near the San Jacinto Fault. Amplitudes of the detected events obey a Gutenberg-Richter distribution with a *b*-value close to one. Foreshocks are common among these detected events, increasing in rate before mainshocks following an inverse Omori's law.

Plain Language Summary We show that an array of over 1,000 seismometers located on a small patch of the San Jacinto Fault in southern California can detect many times more earthquakes than those in standard earthquake catalogs. Although accurate locations cannot be obtained for most of these newly identified events, their amplitudes indicate they obey similar scaling with size as larger magnitude earthquakes. Many of the larger events are preceded by foreshocks and the foreshock rate increases in the time leading up to the mainshocks. Our results suggest that future deployments of small-aperture seismometer arrays could be used to complement existing seismic networks to probe earthquake activity in great detail.

1. Introduction

Detection and location of smaller earthquakes than those routinely processed by local networks are important for illuminating fault structures and describing the temporal evolution of seismicity including swarms and foreshock sequences. To detect small earthquakes, one successful and widely-used technique is the matched-filter approach (i.e., template matching) that detects earthquakes by cross-correlating seismograms of the events in the standard catalog with the continuous waveforms (e.g., Gibbons & Ringdal, 2006; Peng & Zhao, 2009; Ross et al., 2019; Shelly, 2020). This method searches for wave segments that share waveform similarity with the templates (P or S waves) at multiple stations and can lead to 10 times more events than those in conventional catalogs. However, the detections are heavily dependent on the template events already existing in the catalog. To obtain more complete initial event catalogs, other approaches are needed. For example, automated phase-picking algorithms have been developed that are superior to the traditional short-term moving average/long-term moving average (STA/LTA) detection algorithm (Ross & Ben-Zion, 2014; Sleeman & Van Eck, 1999). Recent developments in machine learning have trained deep neural networks using analyst data and provide accurate arrival times of P and S waves that are more consistent than human picks (e.g., Mousavi et al., 2020; Zhu & Beroza, 2019). These improvements in phase detection and timing have led to the identification and characterization of additional earthquakes without requiring templates.

The automated and machine-learning-based picking algorithms are designed to independently work on seismic waveforms recorded by individual stations in a seismic network. When spatially dense arrays are available, array techniques can perform even better in detecting small earthquakes without pre-existing templates. One example is beamforming, which aligns and stacks the waveforms recorded by many seismographs to significantly enhance coherent signals and suppress incoherent noise (e.g., Ben-Zion et al., 2015; Corciulo et al., 2012; Cros et al., 2011; Meng & Ben-Zion, 2018b). Scanning through the continuous stacked waveforms results in many more detections than are visible on single station records, where the signals are often obscured by noise. In this study, we apply beamforming to detect small earthquakes during a 26-day period near an active strand of the San Jacinto fault zone with a dense seismic array of 1,108 vertical nodes.

We detect many times more earthquakes than those documented in the Quake Template Matching (QTM) catalog (Ross et al., 2019) for southern California, currently the most complete earthquake catalog for the region. Ross et al. (2019) applied template matching of known events from 2008 to 2017 to cross-correlate with continuous waveforms from hundreds of stations of the Southern California Seismic Network (SCSN) to find additional events with similar waveforms. The resulting QTM catalog contains about 1.8 million earthquakes, a 10-fold increase compared to the original SCSN catalog. Most of the additional earthquakes are tiny, with magnitudes between zero and −2, but detectable using the computationally intensive waveform cross-correlation method.

Our beam waveforms typically have better signal-to-noise than those recorded by borehole stations for the same events. The observed amplitudes follow a Gutenberg-Richter (G-R) distribution with a *b*-value close to one. Although the exact locations of our newly discovered events are unknown, their P-wave slownesses cluster in groups consistent with QTM catalog locations for events in common. Our expanded event catalog shows that foreshocks among these small earthquakes are relatively common, increasing in rate up to their mainshocks according to an inverse Omori's law.

2. Data

In this study, we perform beamforming analysis to detect coherent signals using the data recorded by a spatially dense seismic array in Southern California. The array consisted of 1,108 vertical 10 Hz nodes centered on the Clark branch of the San Jacinto Fault Zone (SJFZ) at the Sage Brush Flat site (Figure 1). The array recorded velocity seismograms continuously at a 500 Hz sampling rate from 7 May (Julian day 127) 2014 to 13 June (Julian day 164) 2014, and covered approximately a 600 m by 600 m area with a nominal sensor spacing of 10 m perpendicular and 30 m parallel to the fault zone strike (Ben-Zion et al., 2015). These data have been utilized to conduct studies on earthquake detection (e.g., Gradon et al., 2019; Meng & Ben-Zion, 2018b), seismic imaging (e.g., Ben-Zion et al., 2015; Hillers et al., 2016; Mordret et al., 2019; Qin et al., 2018; Roux et al., 2015; Share et al., 2020; Vernon et al., 2014), and anthropogenic and environmental noise sources (e.g., Johnson et al., 2019; Meng & Ben-Zion, 2018a; Zhang et al., 2022).

We also examine the vertical waveforms recorded by seven borehole seismographs within 25 km of the nodal array. These borehole stations have been in continuous operation, recording ground motion at a 100 Hz sampling rate, and we compare these records with the nodal array data to validate detections of earthquakes using the array. The closest borehole instrument, seismograph B946, locates within and beneath the nodal array at a depth of 148 m (Figure 1c).

To reduce the size of the nodal dataset, we decimate the waveforms to 100 Hz, which reduces the data five-fold in size from 1.6 TB to 320 GB. Because all the nodes have the same theoretical response, we do not apply any corrections for instrument response. As performing beamforming analysis on a large dataset is I/O intensive, we convert the hourly waveforms from all the stations into a single binary file to improve computational efficiency. We use non-overlapping 1-hr windows for convenience, accepting that we may lose some event detections in the seconds near each end point.

3. Methods

The spatially dense array is suitable for beamforming analysis to separate coherent and incoherent parts of the continuous seismic records (Rost & Thomas, 2002). To enhance the coherent body waves generated by earthquakes, we apply a slant stacking beamforming algorithm that shifts and stacks waveforms recorded by different

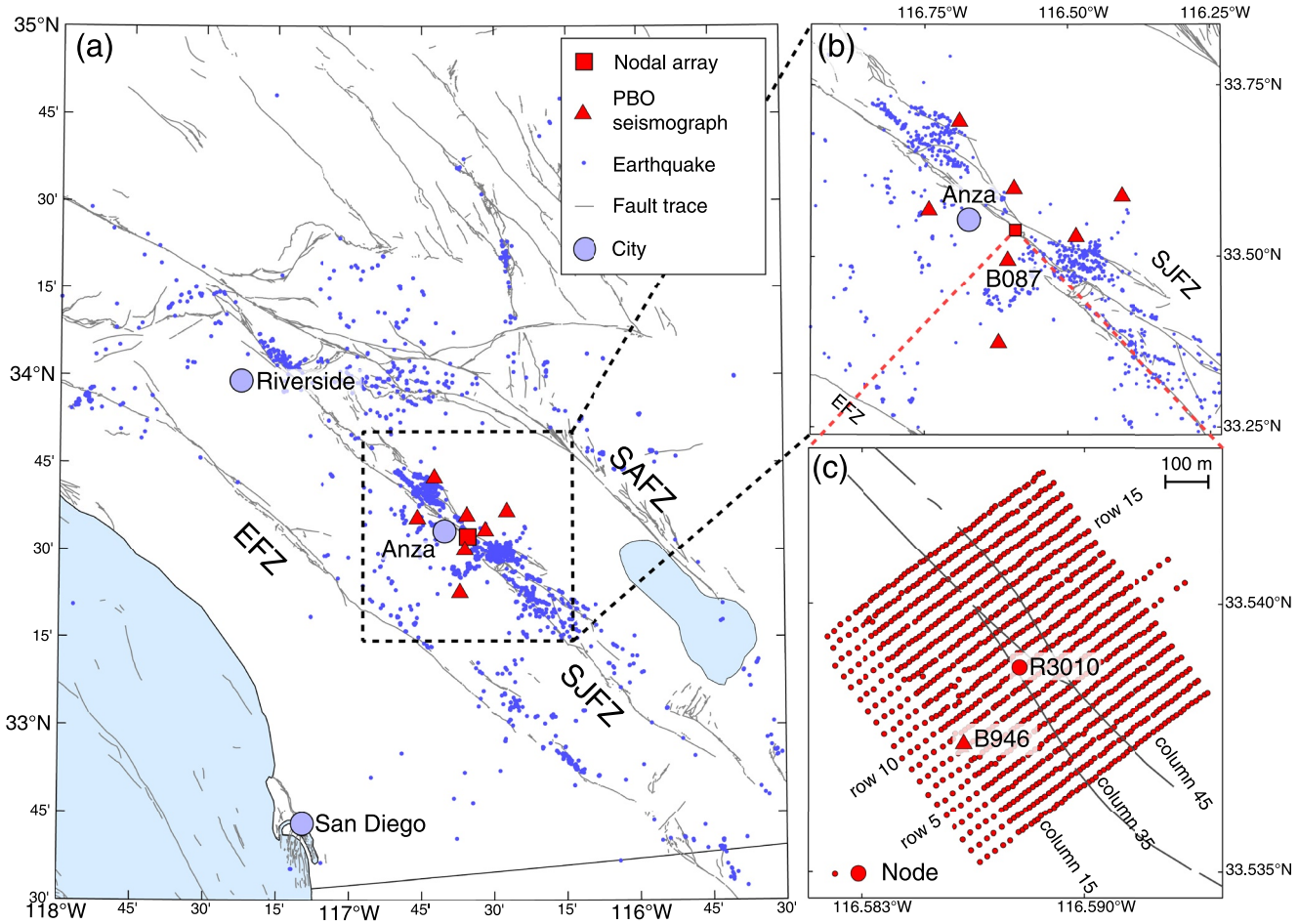

Figure 1. (a) A regional map of Southern California. The red triangles are borehole seismographs. (b) A close-up view of the San Jacinto Fault Zone (SJFZ) near Anza, California. The red square denotes the dense nodal array. The small blue dots are earthquakes documented in the Quake Template Matching (QTM) catalog during the nodal deployment from 10 May 2014 to 3 June 2014. (c) A further zoomed-in view of the dense array with 1,108 nodes at the Sage Brush Flat (SGB) site. The red circles are the nodes, and the red triangle denotes the 148-m-deep borehole seismograph B946.

seismographs using the differential arrival times of an assumed planar wavefront. This is done by predicting the arrival times of the incident wave using a candidate set of slowness vectors. We compute the corresponding ℓ_2 norms of the stacked waveforms for slowness vectors within a uniform slowness grid. The slowness vector yielding the maximum amplitude is used to estimate the direction of the dominant incoming wavefront as a function of time.

Slant stacking in its simplest form assumes that the effects of the 3D velocity structure beneath the array are negligible. In our study, the nodes were located on a fault zone valley with strong horizontal material contrasts and a topographical variation of 100 m (Hillers et al., 2016; Meng & Ben-Zion, 2018b; Mordret et al., 2019; Roux et al., 2015; Share et al., 2020). These lateral variations compromise the waveform alignment in beamforming when only 1D (vertical) variations are assumed. To better align the waveforms, we estimate a correction term for each node using P waves from earthquakes in the QTM catalog.

3.1. Estimating Station Corrections

To obtain station corrections, we compute multichannel cross-correlations of cataloged earthquake P waves to estimate the relative time delays among the stations for each earthquake. Using a 1D velocity model (Hadley & Kanamori, 1977), we first predict the P-wave arrivals at reference station R3010 in the center of the nodal array (Figure 1c) for 798 $M \geq 1$ earthquakes in the QTM catalog (Ross et al., 2019) and then manually refine the arrivals for each earthquake, discarding events with noisy signals. P waves are then extracted at all stations for

0.5 s before and 1.5 s after the arrival and we compute cross-correlations of the P waves of all station pairs. The station corrections are then obtained as the average residual at each station with respect to the 1D velocity model.

Taking an M 1.8 earthquake (Event ID: 15504361; Figure 2) as an example, we cross-correlate the P waves of R3010 and the remaining stations and obtain the maximum cross-correlation coefficients (CC) and corresponding time delays. The P waveforms become less coherent as the inter-station distance increases. Therefore, we only keep station pairs with CC > 0.7 for later analyses. A similar pattern can be obtained when using R2510 as the reference station (Figure S1 of Supporting Information S1). This multichannel cross-correlation approach takes advantage of the entire array and can stably estimate the time delay between two target stations when the waveforms gradually lose coherency with increasing inter-station distance. The time delays of all stations to reference R3010 are then determined using this approach (Figure 2b). By shifting the seismic records according to the time delays, we align and stack the waveforms of the M 1.8 earthquake. Both the S wave and the noise preceding the P arrival are significantly suppressed (Figure 2a). The station corrections for the M 1.8 event are estimated as the residuals between the observed time delays and the 1D model predictions. Note that the array stack with station corrections has larger amplitudes due to the better waveform alignment. The borehole instrument is much more sensitive than the 10-Hz nodal instruments at low frequencies and also records more earthquake energy above about 35 Hz, presumably because it is below the highly attenuating near-surface layer. These differences are illustrated with spectrograms in Figure S2 of Supporting Information S1, which compares the R3010 node record, the nodal array stack, and the borehole station B946 for this M 1.8 event. The array stack has less energy above 20 Hz than the single node and less S-wave energy, likely due to incoherent stacking effects.

Out of the 798 earthquakes, we estimate station corrections for 256 events, each of which yields stable measurements of residuals for more than 200 stations. The resulting median residuals are then used as station corrections for the beamforming analysis (Figure S3a of Supporting Information S1). The station-correction pattern is similar to that estimated using 33 Betsy gunshots during the deployment and a 1D piecewise P-wave velocity model with elevation change (Figures S1 and S3b of Supporting Information S1). The standard deviations of the residuals are smaller for stations closer to the reference station R3010 and the ones with more measurements (Figure S4 of Supporting Information S1). Positive station corrections indicate delayed P waves, and the terms seem to correlate with the local sedimentary basin, the fault damage zone, and the topography (Ben-Zion et al., 2015; Meng & Ben-Zion, 2018b; Share et al., 2020). More details concerning the local topography and the site effects computed from the Betsy gun experiment are in Meng and Ben-Zion (2018b). Here we simply incorporate all of these shallow site corrections, as well as those from deeper structures, into single station terms that describe the integrated P-wave travel-time perturbations from distant earthquakes.

3.2. Beamforming Analysis

For the ith individual station of the nodal array, we denote its location as $\boldsymbol{r}_i$ and its ground motion as a time series $w_i(t)$. To remove the time shift of a plane wavefront with a horizontal slowness vector $\boldsymbol{s}$, we compute

$$\tilde{w}_i(t, \boldsymbol{s}) = w_i(t + \boldsymbol{r}_i \cdot \boldsymbol{s} + \delta t_i), \tag{1}$$

where δt_i is the station correction estimated using earthquake P waves. The beam trace for the entire array with L stations is then calculated using

$$b(t, \boldsymbol{s}) = \frac{1}{L} \sum_{n=1}^{L} \tilde{w}_i(t, \boldsymbol{s}). \tag{2}$$

We compute and later use this linear beam, $b(t, \boldsymbol{s})$, to estimate noise and signal amplitudes. However, for initial event detection, we also applied a more robust beamforming approach that is less sensitive to noise bursts. The dense array frequently recorded noticeable ground motions generated by wind interaction with trees and other surface obstacles (Johnson et al., 2019; Meng et al., 2019). This noise is strong in the frequency band of interest for earthquakes (1–20 Hz) and can be difficult to suppress using the linear stacking approach in Equation 2. To minimize the effect of noise bursts and suppress large amplitude variations, we normalize each trace by its maximum absolute value in each 1-hr time period to decrease the weight of the noisy traces and also apply Nth root stacking of the waveforms to generate the robust beam $\tilde{b}(t, \boldsymbol{s})$:

$$\tilde{b}(t, \boldsymbol{s}) = \frac{1}{L} \sum_{n=1}^{L} |\tilde{w}_i(t, \boldsymbol{s})|^{\frac{1}{N}} \frac{\tilde{w}_i(t, \boldsymbol{s})}{|\tilde{w}_i(t, \boldsymbol{s})|}. \tag{3}$$

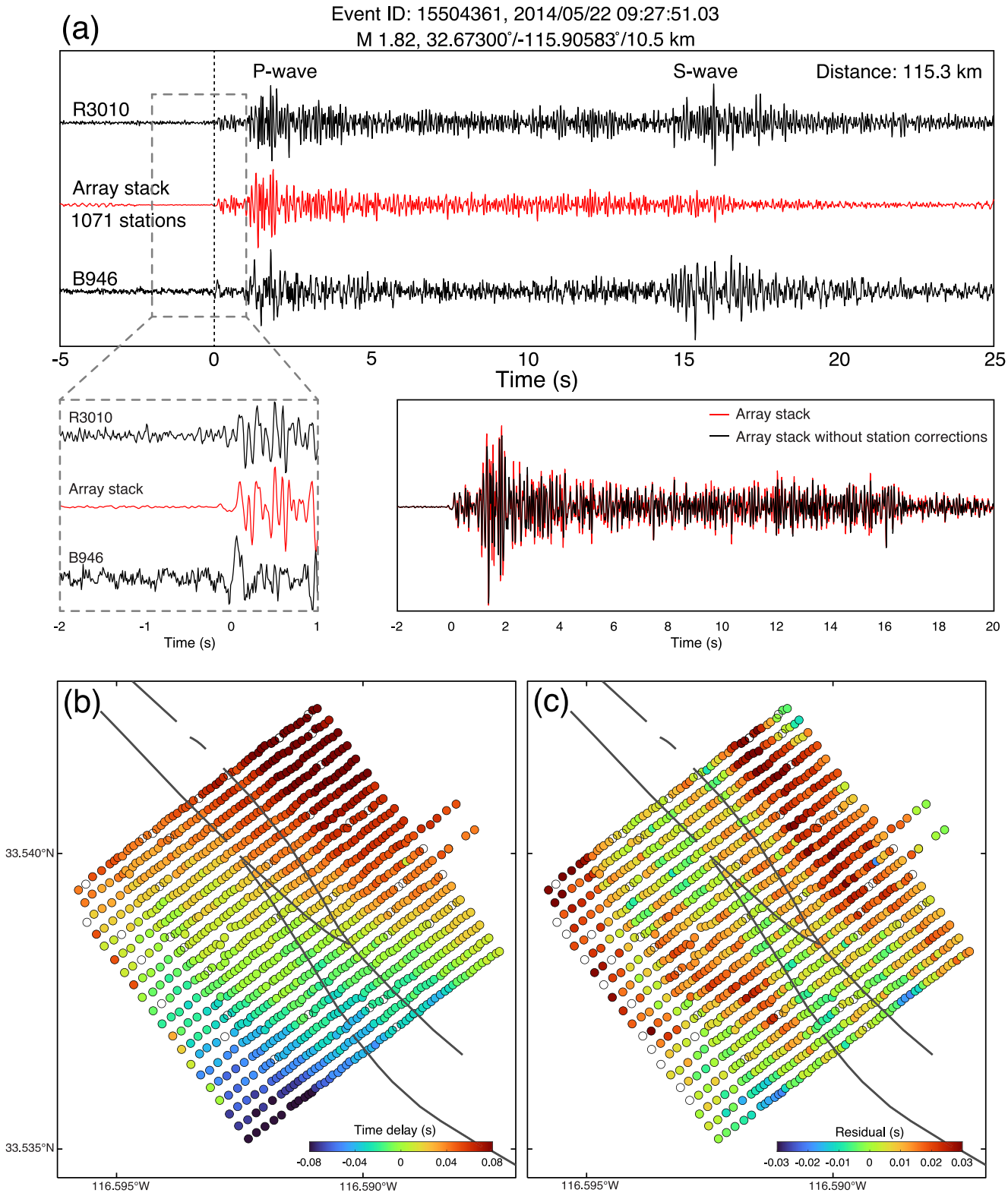

Figure 2.

In this study, we take $N = 2$ such that the stacked waveforms are not overly distorted (Meng & Ben-Zion, 2018b; Rost & Thomas, 2002).

3.3. Event Detection

For event detection, we first compute a time series given by the largest amplitude part of the beam at each time step:

$$s_0(t) = \underset{s \in \boldsymbol{S}}{\operatorname{argmax}}\, \tilde{b}(t, \boldsymbol{s}), \tag{4}$$

where $\boldsymbol{S}$ is the range of slowness $\boldsymbol{s}$. In this study, the east and north components of the slowness vectors range from −0.4 to 0.4 s/km, discretized into 25 samples in each direction. The slowness limit was selected based on the assumption that earthquakes are unlikely to occur in material with a P-wave velocity of less than 2.5 km/s. Slower near-surface velocities are present in some sedimentary basins, but all of the basin velocity profiles in the 3D model of Shaw et al. (2015) have $V_P > 2.5$ km/s below a depth of 1.5 km. We use 996 out of 1,108 stations for the data processing, for which standard deviations of the station corrections are less than 0.02 s (2 samples). The discarded stations are on the edge of the array where the recorded waveforms lose coherency with reference station R3010.

Next, we apply a picking algorithm (Earle & Shearer, 1994) to $\boldsymbol{s_0}$(t) to detect events using a Short-Term-Average (STA) of 0.1 s, a Long-Term-Average (LTA) of 1 s, and a minimum STA/LTA ratio of 1.4. We experimented with applying lower STA/LTA cutoffs, which result in many more detections but visual inspection of these events indicated that they are not as reliable as those seen at ratios of 1.4 or greater. We reject any events with beam slowness greater than 0.35 s/km, which we judge as poorly resolved or likely caused by near-surface noise sources. Our analysis here focuses on the 26 days from 10 May to 4 June 2014 (Julian days 130–155), during which time the array was fully operational. We detect 13,408 events during this period using the autopicker approach. For each event, we search for the maximum beam absolute value over all slowness within 0.5 s of the pick time to estimate the slowness for the event.

To obtain true amplitude information (useful for comparing to catalog magnitudes and estimating b-values), for every detected event from the robust beam, we search the linear beam, $b(t, \boldsymbol{s})$, for its maximum amplitude within 0.5 s of the maximum value of $\tilde{b}(t, \boldsymbol{s})$ at the same slowness. From the linear beam, we also compute pre-event noise measures using a window 2–7 s before the pick time, saving both the maximum noise value over all slowness and the root-mean-square value at the event slowness.

4. Results

4.1. Earthquakes Detected by the Nodal Array

We associated 2,587 of the 13,408 detected events with QTM catalog events (catalog qtm_final_12dev.hypo.txt) based on the fact that their predicted P-wave arrival times (using a 1D velocity model) were within 1.5 s of the pick times from our array beamforming. The validity of many of our detections can be confirmed by comparisons to records from the colocated borehole seismograph B946 (at a depth of 148 m). Figure 3 shows examples of these comparisons for both QTM events and newly detected events. Some detections have clear coherent signals in the array stacks but have amplitudes near the noise level in the borehole records, indicating that beamforming of surface arrays can provide better signal-to-noise than colocated borehole instruments.

Figure 4 shows QTM catalog events during the 26-day time period of our analysis, flagging events that we detected with array beamforming in blue and other events in red. Overall, we detected 55.6% of the events in the QTM catalog for all of Southern California, including 76.0% of those within 30 km of the array, and 66.9%

Figure 2. (a) The black waveforms show the vertical records of a M 1.8 earthquake (Event ID: 15504361; 32.673°, −115.906°, 10.5 km depth) at node R3010 and borehole seismograph B946. The waveforms are bandpass filtered at 0.5–40 Hz with a second-order Butterworth filter. The higher apparent noise level of the borehole instrument is caused by its greater sensitivity at frequencies below about 2 Hz compared to the response of the nodal station R3010. The red waveform in the top panel is the array stack of the 1071 nodal records aligned by cross-correlating the P waves. A closeup of the initial part of the P arrival is shown in the inset panel with increased amplitudes, such that the pre-event noise is more visible. The bottom right panel shows a comparison of the array stack with and without station corrections. (b) Time delays of the P waves of the earthquake are determined by cross-correlation. Reference station R3010 is located in the center of the dense nodal array (Figure 1c). (c) Residuals of the observed and the modeled time delays assuming a planar incoming wave at depth.

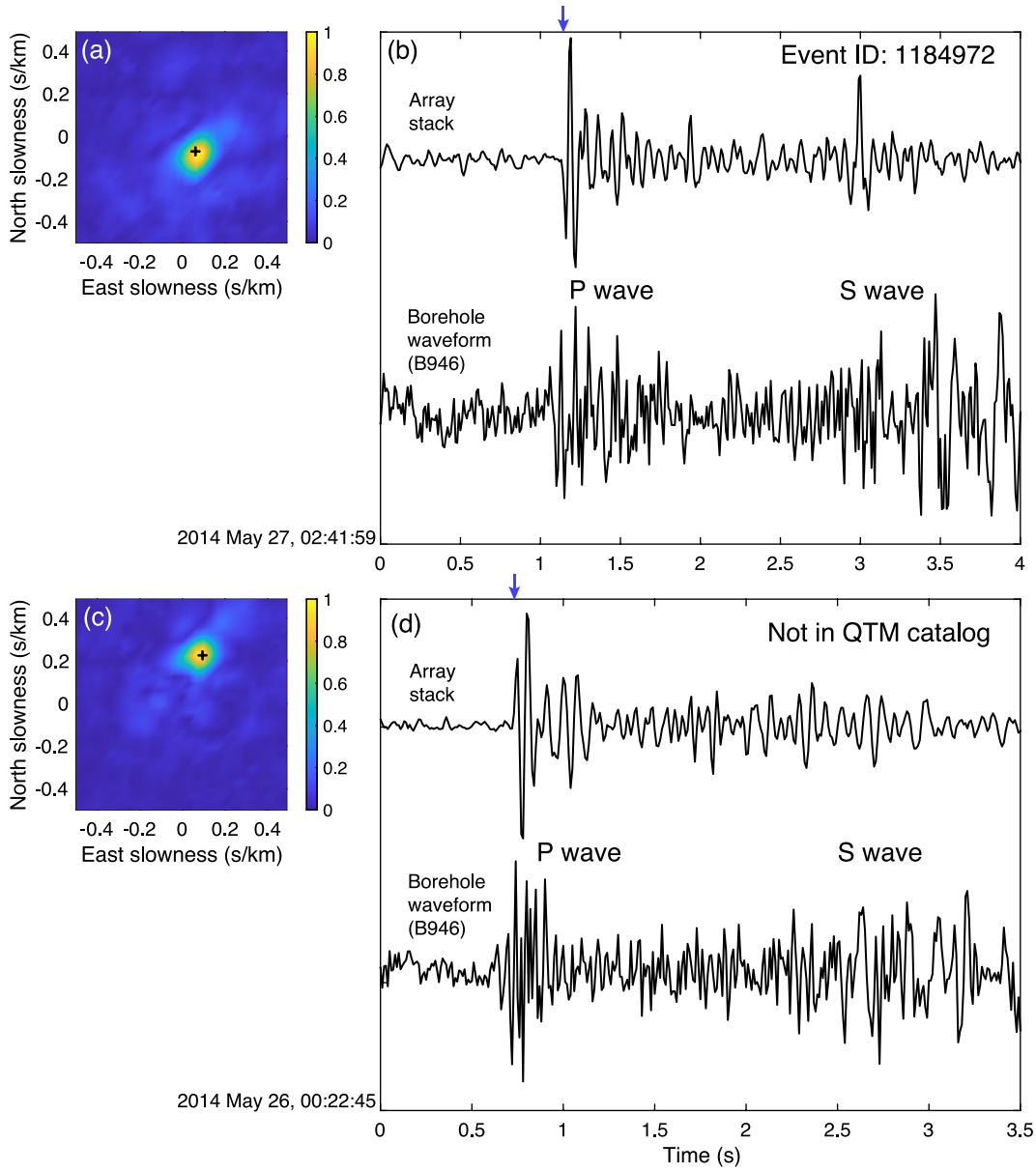

Figure 3. (a) The normalized beam values $\tilde{b}(t, s)$ at the arrival time of the P wave of a quake template matching (QTM) catalog earthquake (Event ID: 1184972). The black cross shows the slowness vector $\boldsymbol{s}_0(t)$ at the maxima of the beamforming diagram. (b) The corresponding vertical waveforms of the array stack (computed for the slowness value indicated by the black cross in the left panel) and a borehole record from station B946. The blue arrow shows the P arrival time. (c) and (d) As above, but for a detected event not in the QTM catalog.

of those within 100 km. Undetected QTM events are not confined to any particular geographic location. Note that the QTM catalog included many events with magnitudes between −1 and 0 within 50 km of the array and beamforming detected most of these events. At longer ranges, the QTM catalog contains mostly magnitude −0.5 and larger events, and not surprisingly, the array beamforming tends to detect more of the larger magnitude events than the smaller magnitudes. For $M > 0.5$ events, we detected 84.8% of those within 30 km and 81.1% of those within 100 km. We found that we could increase the fraction of QTM events detected by lowering the STA/LTA threshold for event detection, but at the cost of lowering the detection reliability, that is, increasing the likelihood of false detections caused by noise features and not earthquakes.

Figure 5a plots the incoming wave slownesses for the array event detections, with QTM-catalog-associated events in blue and 10,545 newly detected events in red. Note that we plot the negative of the slowness vector, s, as

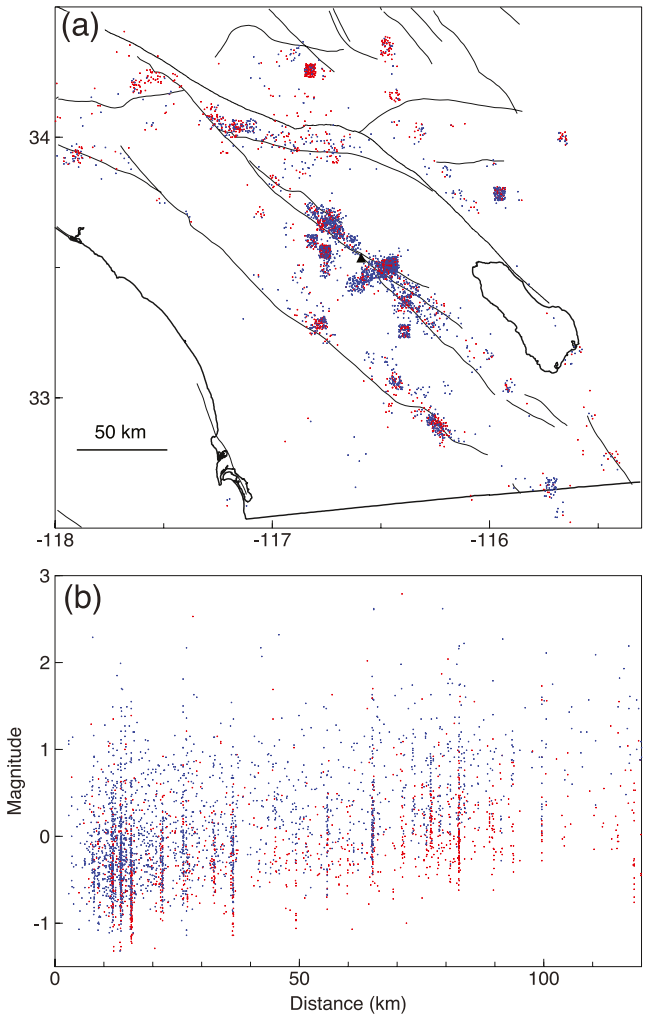

Figure 4. (a) Quake template matching (QTM) catalog events during the 26-day period of our analysis. Random scatter of ±0.025° has been added to each event latitude and longitude for display purposes so that small clusters of seismicity appear as rectangles rather than dots. The 2,587 events detected by our nodal array are plotted in blue; 2,069 non-associated events are in red. The location of the nodal array is shown by the small black triangle in the center of the map. Surface fault traces, the Pacific and Salton Sea shorelines, and the US/Mexico border are also shown. (b) Magnitude versus distance to the center of the nodal array for the QTM catalog for the same time period. Events detected by our nodal array are plotted in blue; non-associated events are in red.

defined in the beamforming section, in order to facilitate comparisons with event locations. Figure 5b shows predicted P-wave slownesses for the QTM events, based on their catalog locations and a 1D velocity model (Hadley & Kanamori, 1977). Individual QTM event clusters can be identified in the observed beam slowness, but their positions are severely distorted, likely caused by local heterogeneities such as the damaged fault zone, fault bi-material interface, and other structures around the nodal array (Ben-Zion et al., 2015; Meng & Ben-Zion, 2018b; Share et al., 2020). Most events from the northwest have apparent incoming directions from the west while events from the southeast have apparent incoming directions to the south (Figure 5b). The observations can be explained by a vertical bi-material interface with a velocity reduction on the northeast side of the SJFZ, which has been observed in multiple fault zone imaging studies (Allam & Ben-Zion, 2012; Qin et al., 2018; Zigone et al., 2015). In this scenario, the early arrivals of detected P waves are mostly from refractions of the faster side, that is, the southwest side, of the fault zone. Without accounting for this heterogeneity, event location estimates obtained solely from the array slowness and S-P times will be significantly biased.

Figure 6 presents the maximum P-wave amplitudes of our detected events, based on the linear beamforming analysis. There is a prominent daily variation in the number of events, with more events detected at night when noise levels are lower. The daily noise variations are likely caused by both anthropogenic activities and wind speed differences. For example, both ground and air traffic can generate incoherent motion across the nodal array in the 1–20 Hz frequency band of interest (Le Gonidec et al., 2021; Meng & Ben-Zion, 2018a; Meng et al., 2021; Zhang et al., 2022). Wind interaction with trees and other surface obstacles is another source of incoherent noise in this frequency band, which can further hinder detecting events during daytime hours (Johnson et al., 2019; Meng et al., 2019). This can be verified by the wind speed recorded by an anemometer installed at the SGB site about 3.5 m above the ground in 2018. The records show faster wind speeds from 8:00 to 19:00 and slower wind speeds during the nighttime hours (Figure S5 of Supporting Information S1). A similar daily variation is also seen in the QTM catalog (Ross et al., 2019). Thus, the ambient noise generated both by anthropogenic activities and wind interactions with surface obstacles modulates the number of earthquakes that can be detected by the dense nodal array as well as the regional network.

Figure 7 plots the number of events as a function of their amplitude, showing that our detected amplitudes obey a power law relation consistent with an earthquake b-value of one, using log(amplitude) for magnitude. As would be expected, the QTM-catalog-associated events form a larger fraction of the high-amplitude detections compared to the low-amplitude detections. Note that our results span a wide range of distances, so the amplitude to magnitude correction term will vary depending on the source location, but our observed slope can still be used to estimate the b-value. For example, consider two different source locations in which event magnitude M is related to amplitude A by $M = k_1 + \log A$ and $M = k_2 + \log A$, respectively. From the G-R relation $\log N = a - bM$, we have

$$N_1 = 10^{a_1 - b(k_1 + \log A)}$$
$$N_2 = 10^{a_2 - b(k_2 + \log A)} \quad (5)$$

in which a_1 and a_2 are the distribution a values (productivity) for the two regions. We then have

$$N = N_1 + N_2 = \left[10^{a_1 - bk_1} + 10^{a_2 - bk_2}\right] 10^{-b \log A} \quad (6)$$

and the resulting $\log N(\log A)$ distribution will have the same slope (b-value) as $\log N(M)$.

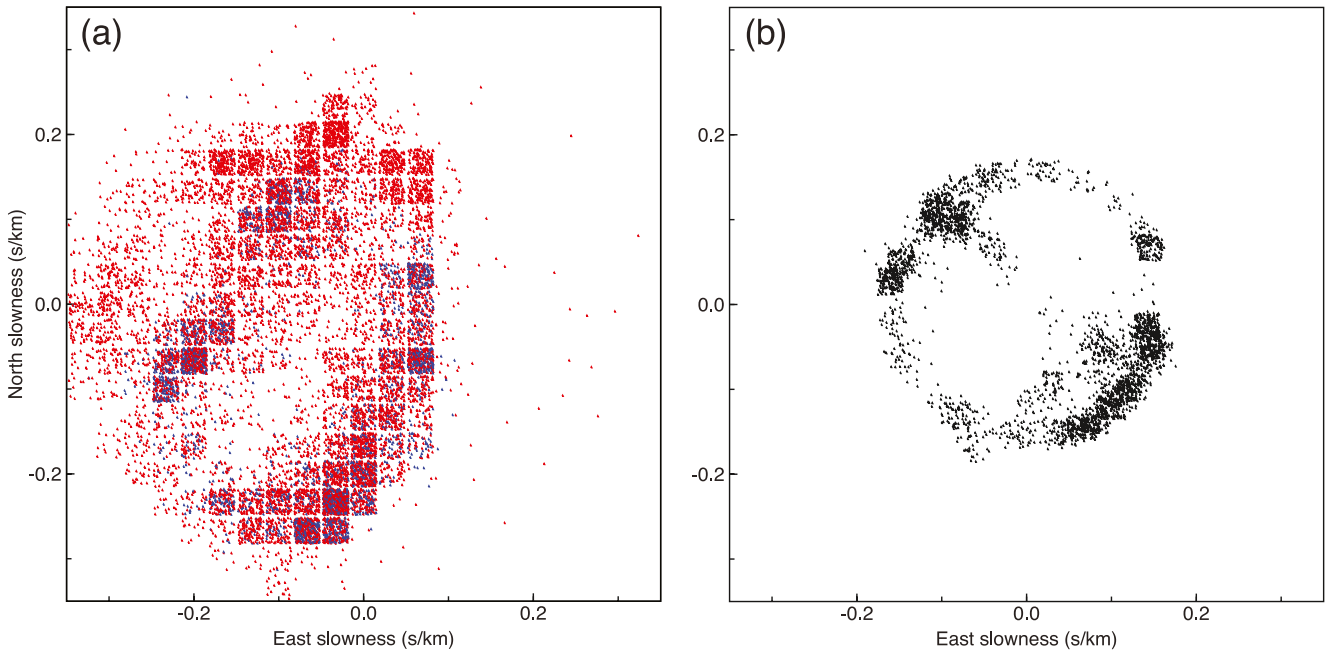

Figure 5. (a) Apparent reverse slowness of the incoming wavefront for 13,408 events detected by the nodal array during 26 days. Quake template matching (QTM) catalog events are plotted in blue, newly detected events are in red. For display purposes, random scatter has been added to the slowness values (computed at only coarse resolution using a grid of slowness values). (b) Theoretical event slownesses for the QTM-associated events, computed based on a 1D velocity model (Hadley & Kanamori, 1977).

Note that this ignores any changes in observed amplitude *b*-value caused by limitations in detection completeness. As discussed by Weiss (1997) for acoustic emission amplitudes, detected events that span a wide range of distances (thus having very different attenuation and geometrical spreading factors) may have an apparent amplitude *b*-value that differs from that of the underlying event magnitude distribution. However, given that our observed log $N(\log A)$ curve is nearly linear over most of its amplitude range with an estimated *b*-value close to expectations for natural seismicity, we do not attempt to test for this possibility here (i.e., by computing separate log $N(\log A)$ distributions for different subregions).

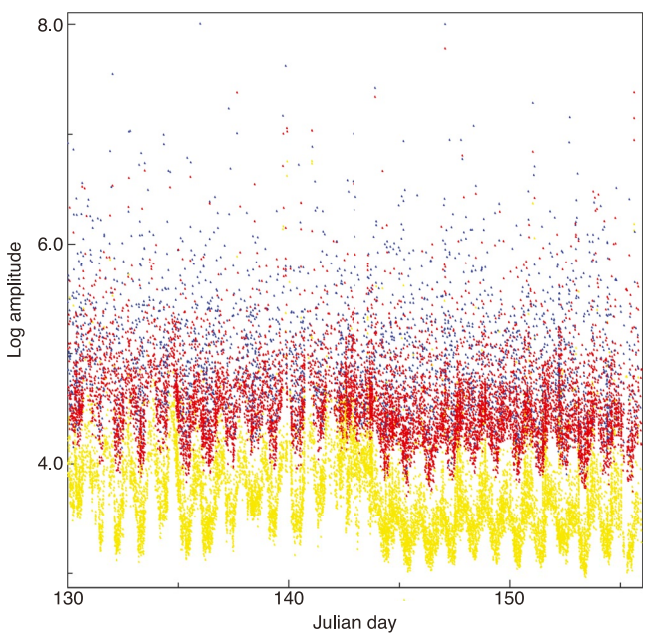

Figure 6. Beam maximum amplitudes for the events detected by the nodal array versus time. Quake template matching catalog associated events are plotted in blue; newly detected events are in red. The yellow dots show the root-mean-square noise level within a window 2–7 s before the P-wave onset.

4.2. Foreshock Activity

Our beamforming detections contain many examples of foreshocks occurring only a few seconds before larger amplitude events, as illustrated in Figure 8. To quantify the average frequency of foreshock occurrence, we search through our catalog of 13,408 event detections and identify 199 "mainshocks" with log(amplitudes) above 6 (see Figure 7) and which have no higher-amplitude events within ±400 s with slowness vector estimates within 0.05 s/km of the target event slowness. We select only these higher amplitude events as mainshocks to ensure that foreshocks with amplitudes of 5% of the mainshock amplitude could still be detected (Figure 7). Their associated foreshocks are identified as preceding events with slowness vectors within 0.05 s/km of the mainshock. We then plot the relative amplitude of any observed foreshocks as a function of time before the target events, as shown in Figure 9. The foreshock rate increases gradually during this 400 s time period, then increases more sharply starting about 15 s before the mainshocks. To examine this rate change, we compute the foreshock rate within 10 intervals equally spaced in log time between $t = -400$ and $t = -3$ s relative to the target mainshock events. For this analysis, we exclude events in the

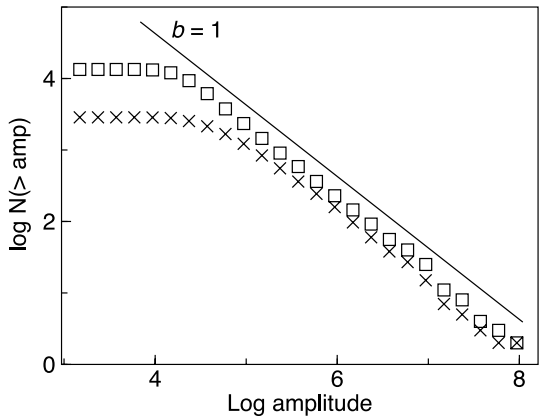

Figure 7. A frequency versus log-amplitude plot for events detected by the beamforming analysis of the nodal array. Results are computed for bins of 0.2 in log amplitude. Squares show all detected events; crosses show the subset of events in the quake template matching catalog. For reference, the plotted line has a slope of −1, corresponding to a *b*-value of one, assuming that log(amplitude) is related to magnitude by a single correction term.

last 3 s before the mainshock to be sure the foreshocks are truly separate and distinct events and not double picks resulting from emergent events or separate P and S phases. We also only include foreshocks with amplitudes greater than 1% of the mainshock amplitude (i.e., above − 2 in Figures 9a and 9b), as the detection rate is less complete for smaller events. Figure 9c plots the resulting foreshock rate versus time in a log-log plot, such that power-law relations will plot as straight lines.

Foreshock sequences are often modeled with empirical earthquake-to-earthquake triggering models. These are informed by statistical models of earthquake catalogs, which derive earthquake-to-earthquake triggering parameters that can explain aftershock sequences. Because an "aftershock" can be larger than the "mainshock," these triggering models (often termed ETAS, for Epidemic Type Aftershock Sequence following Ogata [1988]) predict some degree of foreshock activity in synthetic catalogs. Thus, for comparison we also plot predicted foreshock rates for the self-similar ETAS model described in Shearer (2012a, 2012b) resulting from a simulation of 300,000 background events. We generate a synthetic catalog of triggered sequences assuming a *b*-value of 1, Omori's law parameters $p = 1$, $c = 1$ s, minimum and maximum magnitudes of 0 and 5.5, respectively,

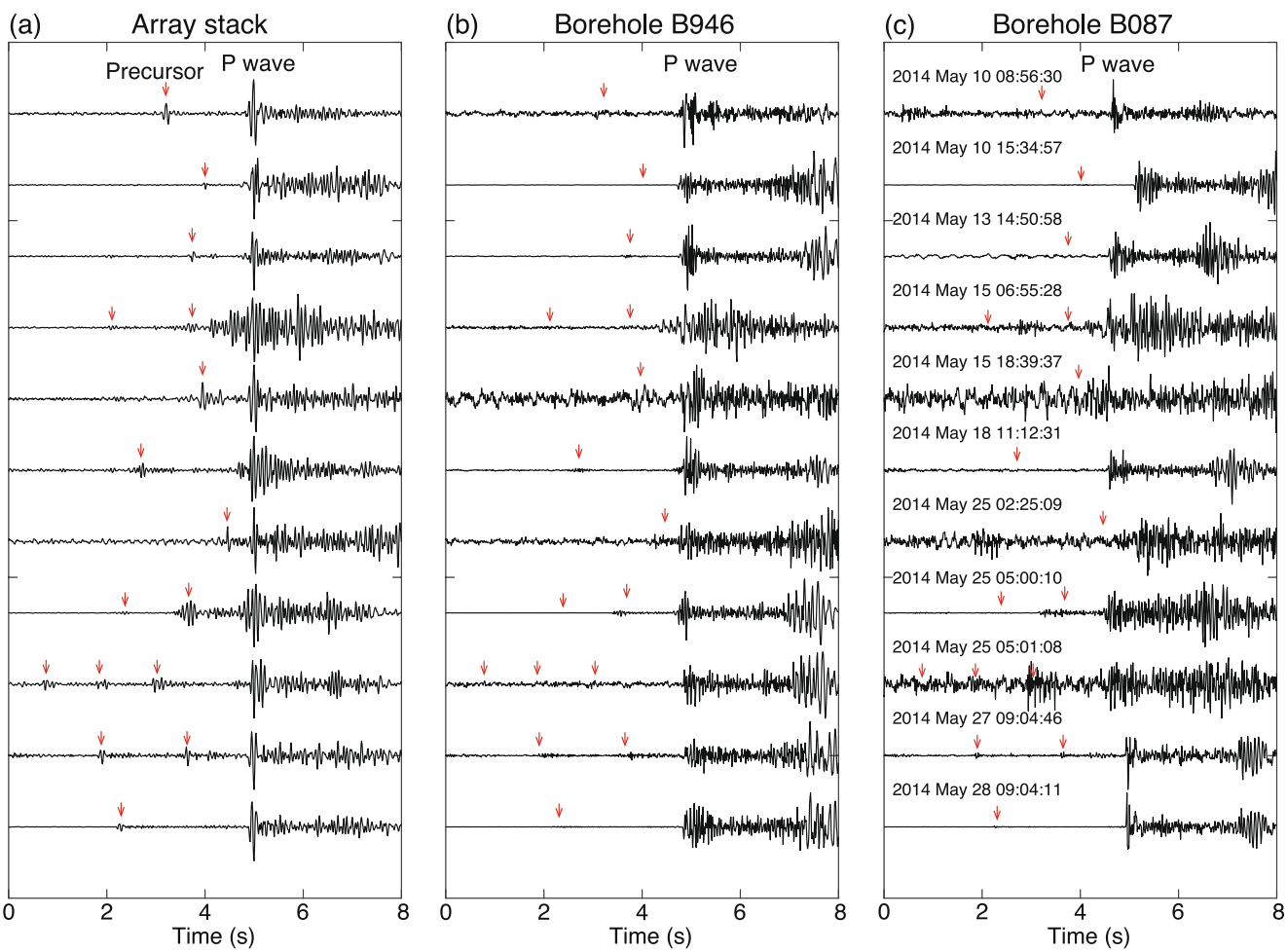

Figure 8. (a) Examples of foreshocks detected using the nodal array. Seismic precursors (foreshocks) are highlighted by the red arrows. (b) The corresponding vertical records are from the borehole seismograph B946, located within the nodal array. (c) Vertical records from the borehole seismograph B087, located 9 km away. Event times are labeled.

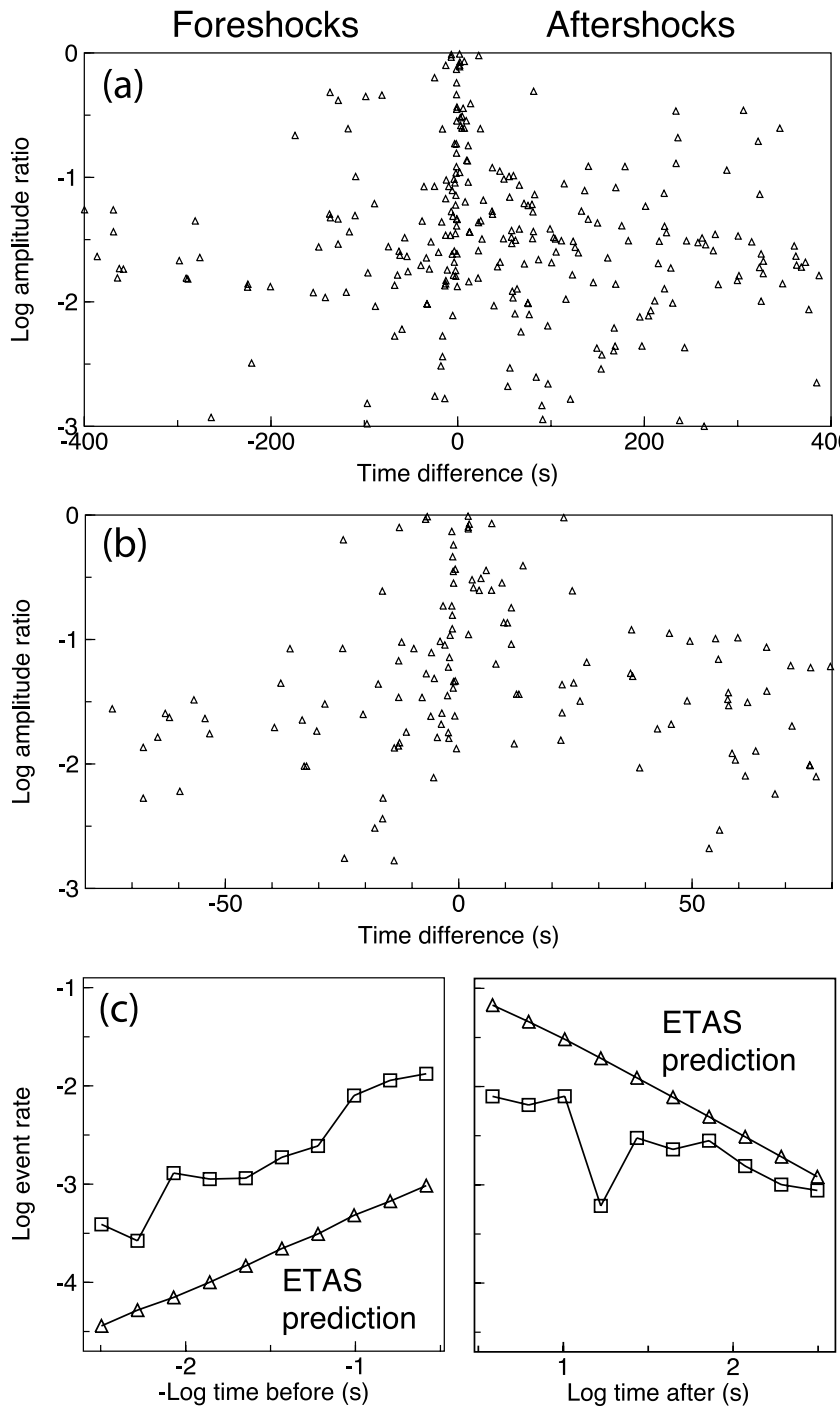

Figure 9. (a) Foreshock/mainshock and aftershock/mainshock amplitudes as a function of time for 400 s before and after 199 target mainshocks among the events detected by the nodal array. (b) A closeup showing the 80 s before and after the mainshocks. Note the increasing foreshock activity rate with time, especially in the last 15 s. (c) Squares plot observed log event rate (number of foreshocks and aftershocks per target event per second) computed for equally spaced bins in log(time) before and after the mainshock. Only events with log amplitude ratios above −2 are included. The triangles show predictions based on an epidemic type aftershock sequence (ETAS)-type earthquake triggering model (see text). Note that the observed foreshock rate greatly exceeds the ETAS model predictions while the observed aftershock rate is less than the ETAS predictions.

minimum and maximum time delays of 1 s and 30,000 s respectively, and an aftershock productivity parameter Q of 0.031 (corresponding to a branching ratio of 0.39). As explained in Shearer (2012a), this value of Q with our assigned magnitude range yields sequences that obey Båth's law (Båth, 1965), that is the largest aftershock is on average 1.2 magnitudes smaller than its mainshock. We then mimic the processing of our event detections by searching for target events above M 2 within the sequences that do not have larger magnitude events within ±400 s and count the foreshocks that are greater than 2 magnitude units smaller than the target mainshocks. Note that the synthetic foreshock rates are much less than observed rates but the growth in foreshock rate, that is, the inverse of Omori's law (Helmstetter et al., 2003; Jones & Molnar, 1979; Maeda, 1999; Ogata & Katsura, 2014; Peng et al., 2007), is roughly comparable.

For comparison to the foreshock numbers, we also estimate aftershock rates from the same set of 199 "mainshock" events. Their associated aftershocks are identified as following events within 400 s with slowness vectors within 0.05 s/km of the mainshock. Relative amplitudes of these events are plotted as a function of time in Figure 9. Because of higher noise levels from the mainshock coda we likely miss many aftershocks in the first 10 to 30 seconds. Figure 9c plots observed aftershock rate versus time in a log-log plot compared to predictions of our ETAS model. Note that the observed aftershock rate begins to approach the ETAS predictions at longer times, where the obscuring effects of the mainshock coda are absent. In general, the observed foreshock and aftershock rates are much closer (i.e., more time symmetric) than the predictions of the ETAS model, similar to previous observations based on the SCSN catalog (Brodsky, 2011; Shearer, 2012b).

Because we cannot locate most of our detected events, the requirement that the foreshocks have similar slowness vectors to their associated mainshocks does not guarantee close physical proximity. Thus, our results are likely more contaminated by "background" activity, that is, random events that are not spatially related to the target events, than foreshock studies that use catalog locations. However, the rate of background seismicity distant from the target events should be uncorrelated in time with target event occurrence, so the observed increase in rate with time leading up to the mainshocks suggests that any bias caused by the location uncertainty is small.

5. Discussion

Our results demonstrate that it is possible to use a dense nodal array of hundreds of sensors on the SJFZ to detect many times more earthquakes in southern California than those in standard catalogs, even those computed using template matching. However, because of the location of the array directly spanning the San Jacinto fault, the observed directions of the incoming P-waves are severely distorted by 3D velocity heterogeneity. This likely reduces the coherence of our beamforming even after applying station corrections and hampers the use of slowness information to estimate event locations. Since many of our detected events are in the QTM catalog, it should be possible to use array beam records from these events as templates to cross-correlate with other array detections to identify additional detected events in nearly the same locations. However, with only a single array, there will always be considerable location uncertainty with this approach.

In principle, S-wave detections could be used to better resolve event locations using only the nodal array data. Although S-waves are often seen (e.g., Figures 2 and 3), they are difficult to resolve and time for the majority of our detected events. This is likely due to the vertical component instruments as well as the fact that our station corrections and beam stacking are based on P-wave alignments. A separate analysis focused on S-waves would likely improve their visibility, but we defer this to future work.

Much more accurate earthquake locations could be achieved for these tiny earthquakes using multiple nodal arrays suitably situated around areas of active seismicity. Although nodal experiments are often conducted along faults to resolve low-velocity zones, fault-guided waves, and other near-fault phenomena, the best imaging of deep fault seismicity will likely be achieved with off-fault arrays that enjoy a "clean" view from the side, relatively undistorted by along-fault heterogeneity. The arrays should have an aperture ≤1 km to ensure the coherence of the recorded waveforms. Our results suggest that such arrays will be effective even at a considerable distance from the faults, as we detected about half of the events in the QTM catalog at distances between 90 and 110 km.

We analyzed all 1,108 stations of the nodal array at the Sage Brush Flat site on the SJFZ, but it's not clear if this many stations are required for event detection purposes or if the array geometry is optimal. Thus, some experimentation with analysis of subsets of the 1,108 stations, which span a range of array dimensions, would help in planning future experiments focused on event detection. In addition, the use of three-component arrays should

be considered to yield better S-wave information that would help in locating events. Finally, we applied a fairly simple beamforming and STA/LTA detector approach. Template matching or other more advanced detection algorithms could likely pull out even more earthquakes from these data.

Foreshock studies benefit from having as complete a catalog as possible, that is, one containing many small earthquakes that are below the standard detection threshold. In southern California, this has been achieved using both template matching (Ross et al., 2019) and machine learning (Ross & Cochran, 2021; Ross et al., 2020), which has enabled swarm and foreshock studies that probe deeper into earthquake behavior than standard catalogs (e.g., Ross & Cochran, 2021; Ross et al., 2020; Trugman & Ross, 2019). Our results show that beamforming data from a large-N array can detect over 10,000 more events than the template-matched QTM catalog over a 26-day period, at least for our array on an active section of the San Jacinto Fault. We detect almost 3 times the number of events in the QTM catalog across all of southern California and we identify many foreshocks among these small events.

A key question regarding foreshocks is whether their occurrence rates are comparable to those predicted by ETAS triggering models based on aftershock statistics. Some studies (e.g., Felzer et al., 2004; Helmstetter et al., 2003; Helmstetter & Sornette, 2003; Marzocchi & Zhuang, 2011) have suggested that foreshock and aftershock statistics are consistent with a single triggering model in which foreshocks are simply events that generate unusually large aftershocks (i.e., with magnitudes greater than the triggering event). However, more recent work (e.g., Brodsky, 2011; Chen & Shearer, 2016; Petrillo & Lippiello, 2021; Seif et al., 2019; Shearer, 2012a, 2012b) has documented a surplus of foreshocks in observed earthquake catalogs compared to ETAS predictions. The greatly expanded southern California earthquake catalog computed using template matching (Ross et al., 2019) has been the focus of several recent foreshock studies with Trugman and Ross (2019) finding that 72% of 46 $M \geq 4$ mainshocks are preceded by foreshock activity. However, van den Ende and Ampuero (2020) argued, based on a different model to define background seismicity, that a much smaller fraction of the QTM mainshocks considered by Trugman and Ross (2019) are proceeded by statistically significant increases in seismicity rate and Moutote et al. (2021) claimed that only three of the QTM mainshocks have foreshock activity that exceeds that expected from fluctuations in background rate and ETAS predictions.

The statistical models that define these arguments benefit from expanded catalogs that include more of the tiny earthquakes that can help resolve foreshock and aftershock behavior for smaller mainshocks. As noted above, we are detecting many more earthquakes than in the QTM catalog and our observations suggest that foreshocks are seen even for the smaller amplitude events in our catalog. When comparing our detected event amplitudes to a specific self-similar ETAS model designed by Shearer (2012a) to fit Båth's law, we find that they both obey an inverse Omori's law but that our observations indicate a surplus of foreshocks and a higher ratio of foreshocks to aftershocks compared to model predictions, consistent with the findings of more comprehensive southern California foreshock studies (Brodsky, 2011; Chen & Shearer, 2016; Petrillo & Lippiello, 2021; Seif et al., 2019; Shearer, 2012a, 2012b). However, we do not have true magnitude estimates and we have not explored different ETAS models so an ETAS-like model may exist that could fit our observations, particularly since we have focused on only a limited time period (400 s) before the mainshocks. We defer a more comprehensive search of ETAS parameter space for future work, which ideally would explore models that can fit both our observations and those of other southern California earthquake catalogs.

We find many foreshocks among the events we detect with the nodal array, a result with some similarities to an autocorrelation analysis of earthquakes in the 2019 Ridgecrest earthquake sequence, which found many examples of foreshocks in the 100 s before their mainshocks (Meng & Fan, 2021). It remains to be seen whether these foreshock results are specific to the Ridgecrest and San Jacinto fault study regions and time periods or if they reflect more widespread behavior. Nonetheless, accelerating foreshock activity immediately before mainshocks that exceed that expected from ETAS-like models, if confirmed, would have important implications for models of foreshock behavior. It is unclear whether anomalously high foreshock rates can be explained with models in which both swarms and foreshock sequences are both driven by similar mechanisms, such as a slow slip or fluid migration. In particular, an acceleration in foreshock activity appears more consistent with rupture cascade and nucleation phase models, which involve a closer physical link between the foreshock activity and the mainshock rupture (e.g., Bouchon et al., 2013; Kanamori & Cipar, 1974; Liu et al., 2020; Ohnaka, 1992). One idea involves a hierarchical nucleation process in which the observed earthquakes result from a cascade of triggered slip patches (Abercrombie & Mori, 1994; Ellsworth & Bulut, 2018; Fukao & Furumoto, 1985; Ide, 2019; Okuda

& Ide, 2018; Wyss & Brune, 1967). In this model, foreshocks trigger each other by generating stress perturbations in the surrounding area and eventually initiate the rupture of the mainshock. Alternatively, foreshocks could be triggered by propagating aseismic slip (Dodge et al., 1996; Ellsworth & Beroza, 1995; McLaskey, 2019), with seismicity migrating around the earthquake epicenter before the fault slip reaches a critical size (Lapusta & Rice, 2003; Tape et al., 2018). In this case, the foreshocks reflect a time-dependent failure process, often termed the nucleation phase, that culminates in the mainshock.

These mechanisms are not completely independent. For example, ETAS-like triggering is likely caused by static or dynamic stress changes that increase the chances of subsequent nearby earthquakes. Similarly, a rupture cascade might lead to a mainshock nucleation phase. Which mechanism dominates rupture initiation and development in nature has been debated for decades. For example, Dodge et al. (1996) investigated foreshock sequences of six M 4.7 to 7.3 earthquakes and found that the foreshocks suggest an aseismic nucleation process. However, five out of these six target earthquakes were also analyzed by Abercrombie and Mori (1996) in a study of foreshock occurrence patterns associated with 59 $M \geq 5$ earthquakes in the western US, which argued the foreshocks are likely not part of an earthquake nucleation process. Similar studies of the 1999 Hector Mine and 1999 Izmit earthquakes have reached differing conclusions (Bouchon et al., 2011; Chen & Shearer, 2013; Ellsworth & Bulut, 2018; Yoon et al., 2019).

Resolving among these different foreshock/mainshock models from our observations is difficult because we lack precise locations that could be used to determine how far the foreshocks are from the mainshock hypocenters and whether the foreshocks migrate toward the mainshock. We hope, however, that our results will motivate future studies of the San Jacinto and other faults using multiple nodal arrays or other methods to detect and locate thousands of tiny earthquakes that may hold the key to understanding important questions concerning how earthquake activity evolves in time and space.

Data Availability Statement

The seismic records were provided by the Data Management Center (DMC) of the Incorporated Research Institutions for Seismology (IRIS) and the SCEDC (Caltech.Dataset, 2013). The nodal array data is openly available through the IRIS DMC (https://doi.org/10.7914/SN/ZG_2014; Vernon et al., 2014). The QTM catalog is from SCEDC (https://scedc.caltech.edu/data/qtm-catalog.html; Ross et al., 2019). The 1D velocity model used in this study is from SCEC (https://strike.scec.org/scecpedia/Hadley-Kanamori; Hadley & Kanamori, 1977).

Acknowledgments
We thank reviewers for constructive suggestions and comments that improved the paper. Funding for this research was provided by NEHRP/USGS Grant G20AP0027 and by SCEC under Grant 20097. SCEC is funded by NSF Cooperative Agreement EAR-1033462 and USGS Cooperative Agreement G12AC20038. This is SCEC contribution 11883.

References

Abercrombie, R. E., & Mori, J. (1994). Local observations of the onset of a large earthquake: 28 June 1992 Landers, California. *Bulletin of the Seismological Society of America*, *84*(3), 725–734.

Abercrombie, R. E., & Mori, J. (1996). Occurrence patterns of foreshocks to large earthquakes in the Western United States. *Nature*, *381*(6580), 303–307. https://doi.org/10.1038/381303a0

Allam, A., & Ben-Zion, Y. (2012). Seismic velocity structures in the southern California plate-boundary environment from double-difference tomography. *Geophysical Journal International*, *190*(2), 1181–1196. https://doi.org/10.1111/j.1365-246x.2012.05544.x

Båth, M. (1965). Lateral inhomogeneities of the upper mantle. *Tectonophysics*, *2*(6), 483–514. https://doi.org/10.1016/0040-1951(65)90003-x

Ben-Zion, Y., Vernon, F. L., Ozakin, Y., Zigone, D., Ross, Z. E., Meng, H., et al. (2015). Basic data features and results from a spatially dense seismic array on the San Jacinto fault zone. *Geophysical Journal International*, *202*(1), 370–380. https://doi.org/10.1093/gji/ggv142

Bouchon, M., Durand, V., Marsan, D., Karabulut, H., & Schmittbuhl, J. (2013). The long precursory phase of most large interplate earthquakes. *Nature Geoscience*, *6*(4), 299–302. https://doi.org/10.1038/ngeo1770

Bouchon, M., Karabulut, H., Aktar, M., Özalaybey, S., Schmittbuhl, J., & Bouin, M.-P. (2011). Extended nucleation of the 1999 Mw 7.6 Izmit earthquake. *Science*, *331*(6019), 877–880. https://doi.org/10.1126/science.1197341

Brodsky, E. E. (2011). The spatial density of foreshocks. *Geophysical Research Letters*, *38*(10), L10305. https://doi.org/10.1029/2011gl047253

Caltech. Dataset. (2013). Southern California earthquake data center. https://doi.org/10.7909/C3WD3xH1

Chen, X., & Shearer, P. M. (2013). California foreshock sequences suggest aseismic triggering process. *Geophysical Research Letters*, *40*(11), 2602–2607. https://doi.org/10.1002/grl.50444

Chen, X., & Shearer, P. M. (2016). Analysis of foreshock sequences in California and implications for earthquake triggering. *Pure and Applied Geophysics*, *173*(1), 133–152. https://doi.org/10.1007/s00024-015-1103-0

Corciulo, M., Roux, P., Campillo, M., & Dubucq, D. (2012). Instantaneous phase variation for seismic velocity monitoring from ambient noise at the exploration scale. *Geophysics*, *77*(4), Q37–Q44. https://doi.org/10.1190/geo2011-0363.1

Cros, E., Roux, P., Vandemeulebrouck, J., & Kedar, S. (2011). Locating hydrothermal acoustic sources at Old Faithful Geyser using matched field processing. *Geophysical Journal International*, *187*(1), 385–393. https://doi.org/10.1111/j.1365-246x.2011.05147.x

Dodge, D. A., Beroza, G. C., & Ellsworth, W. (1996). Detailed observations of California foreshock sequences: Implications for the earthquake initiation process. *Journal of Geophysical Research*, *101*(B10), 22371–22392. https://doi.org/10.1029/96jb02269

Earle, P. S., & Shearer, P. M. (1994). Characterization of global seismograms using an automatic-picking algorithm. *Bulletin of the Seismological Society of America*, *84*(2), 366–376. https://doi.org/10.1785/bssa0840020366

Ellsworth, W. L., & Beroza, G. (1995). Seismic evidence for an earthquake nucleation phase. *Science*, *268*(5212), 851–855. https://doi.org/10.1126/science.268.5212.851

Ellsworth, W. L., & Bulut, F. (2018). Nucleation of the 1999 Izmit earthquake by a triggered cascade of foreshocks. *Nature Geoscience*, *11*(7), 531–535. https://doi.org/10.1038/s41561-018-0145-1

Felzer, K. R., Abercrombie, R. E., & Ekstrom, G. (2004). A common origin for aftershocks, foreshocks, and multiplets. *Bulletin of the Seismological Society of America*, *94*(1), 88–98. https://doi.org/10.1785/0120030069

Fukao, Y., & Furumoto, M. (1985). Hierarchy in earthquake size distribution. *Physics of the Earth and Planetary Interiors*, *37*(2–3), 149–168. https://doi.org/10.1016/0031-9201(85)90048-2

Gibbons, S. J., & Ringdal, F. (2006). The detection of low magnitude seismic events using array-based waveform correlation. *Geophysical Journal International*. https://doi.org/10.1111/j.1365-246x.2006.02865.x

Gradon, C., Moreau, L., Roux, P., & Ben-Zion, Y. (2019). Analysis of surface and seismic sources in dense array data with match field processing and Markov chain Monte Carlo sampling. *Geophysical Journal International*, *218*(2), 1044–1056. https://doi.org/10.1093/gji/ggz224

Hadley, D., & Kanamori, H. (1977). Seismic structure of the Transverse ranges, California. *The Geological Society of America Bulletin*, *88*(10), 1469–1478. https://doi.org/10.1130/0016-7606(1977)88<1469:ssottr>2.0.co;2

Helmstetter, A., & Sornette, D. (2003). Foreshocks explained by cascades of triggered seismicity. *Journal of Geophysical Research*, *108*(B10). https://doi.org/10.1029/2003jb002409

Helmstetter, A., Sornette, D., & Grasso, J.-R. (2003). Mainshocks are aftershocks of conditional foreshocks: How do foreshock statistical properties emerge from aftershock laws. *Journal of Geophysical Research*, *108*(B1). https://doi.org/10.1029/2002jb001991

Hillers, G., Roux, P., Campillo, M., & Ben-Zion, Y. (2016). Focal spot imaging based on zero lag cross-correlation amplitude fields: Application to dense array data at the San Jacinto fault zone. *Journal of Geophysical Research: Solid Earth*, *121*(11), 8048–8067. https://doi.org/10.1002/2016jb013014

Ide, S. (2019). Frequent observations of identical onsets of large and small earthquakes. *Nature*, *573*(7772), 112–116. https://doi.org/10.1038/s41586-019-1508-5

Johnson, C. W., Meng, H., Vernon, F., & Ben-Zion, Y. (2019). Characteristics of ground motion generated by wind interaction with trees, structures, and other surface obstacles. *Journal of Geophysical Research: Solid Earth*, *124*(8), 8519–8539. https://doi.org/10.1029/2018jb017151

Jones, L. M., & Molnar, P. (1979). Some characteristics of foreshocks and their possible relationship to earthquake prediction and premonitory slip on faults. *Journal of Geophysical Research*, *84*(B7), 3596–3608. https://doi.org/10.1029/jb084ib07p03596

Kanamori, H., & Cipar, J. J. (1974). Focal process of the great Chilean earthquake May 22, 1960. *Physics of the Earth and Planetary Interiors*, *9*(2), 128–136. https://doi.org/10.1016/0031-9201(74)90029-6

Lapusta, N., & Rice, J. R. (2003). Nucleation and early seismic propagation of small and large events in a crustal earthquake model. *Journal of Geophysical Research*, *108*(B4). https://doi.org/10.1029/2001jb000793

Le Gonidec, Y., Kergosien, B., Wassermann, J., Jaeggi, D., & Nussbaum, C. (2021). Underground traffic-induced body waves used to quantify seismic attenuation properties of a bimaterial interface nearby a main fault. *Journal of Geophysical Research: Solid Earth*, *126*(8), e2021JB021759. https://doi.org/10.1029/2021jb021759

Liu, Y., McGuire, J. J., & Behn, M. D. (2020). Aseismic transient slip on the Gofar transform fault, East Pacific Rise. *Proceedings of the National Academy of Sciences*, *117*(19), 10188–10194. https://doi.org/10.1073/pnas.1913625117

Maeda, K. (1999). Time distribution of immediate foreshocks obtained by a stacking method. *Pure and Applied Geophysics*, *155*(2), 381–394. https://doi.org/10.1007/978-3-0348-8677-2_9

Marzocchi, W., & Zhuang, J. (2011). Statistics between mainshocks and foreshocks in Italy and southern California. *Geophysical Research Letters*, *38*(9). https://doi.org/10.1029/2011gl047165

McLaskey, G. C. (2019). Earthquake initiation from laboratory observations and implications for foreshocks. *Journal of Geophysical Research: Solid Earth*, *124*(12), 12882–12904. https://doi.org/10.1029/2019jb018363

Meng, H., & Ben-Zion, Y. (2018a). Characteristics of airplanes and helicopters recorded by a dense seismic array near Anza California. *Journal of Geophysical Research: Solid Earth*, *123*(6), 4783–4797. https://doi.org/10.1029/2017jb015240

Meng, H., & Ben-Zion, Y. (2018b). Detection of small earthquakes with dense array data: Example from the San Jacinto fault zone, southern California. *Geophysical Journal International*, *212*(1), 442–457. https://doi.org/10.1093/gji/ggx404

Meng, H., Ben-Zion, Y., & Johnson, C. W. (2019). Detection of random noise and anatomy of continuous seismic waveforms in dense array data near Anza California. *Geophysical Journal International*, *219*(3), 1463–1473. https://doi.org/10.1093/gji/ggz349

Meng, H., Ben-Zion, Y., & Johnson, C. W. (2021). Analysis of seismic signals generated by vehicle traffic with application to derivation of subsurface Q-values. *Seismological Research Letters*, e2021GL095704. https://doi.org/10.1785/0220200457

Meng, H., & Fan, W. (2021). Immediate foreshocks indicating cascading rupture developments for 527 m 0.9 to 5.4 Ridgecrest earthquakes. *Geophysical Research Letters*, *48*(19), e2021GL095704. https://doi.org/10.1029/2021gl095704

Mordret, A., Roux, P., Boué, P., & Ben-Zion, Y. (2019). Shallow three-dimensional structure of the San Jacinto fault zone revealed from ambient noise imaging with a dense seismic array. *Geophysical Journal International*, *216*(2), 896–905. https://doi.org/10.1093/gji/ggy464

Mousavi, S. M., Ellsworth, W. L., Zhu, W., Chuang, L. Y., & Beroza, G. C. (2020). Earthquake transformer—An attentive deep-learning model for simultaneous earthquake detection and phase picking. *Nature Communications*, *11*(1), 1–12. https://doi.org/10.1038/s41467-020-17591-w

Moutote, L., Marsan, D., Lengliné, O., & Duputel, Z. (2021). Rare occurrences of non-cascading foreshock activity in southern California. *Geophysical Research Letters*, *48*(7), e2020GL091757. https://doi.org/10.1029/2020gl091757

Ogata, Y. (1988). Statistical models for earthquake occurrences and residual analysis for point processes. *Journal of the American Statistical Association*, *83*(401), 9–27. https://doi.org/10.1080/01621459.1988.10478560

Ogata, Y., & Katsura, K. (2014). Comparing foreshock characteristics and foreshock forecasting in observed and simulated earthquake catalogs. *Journal of Geophysical Research: Solid Earth*, *119*(11), 8457–8477. https://doi.org/10.1002/2014jb011250

Ohnaka, M. (1992). Earthquake source nucleation: A physical model for short-term precursors. *Tectonophysics*, *211*(1–4), 149–178. https://doi.org/10.1016/0040-1951(92)90057-d

Okuda, T., & Ide, S. (2018). Hierarchical rupture growth evidenced by the initial seismic waveforms. *Nature Communications*, *9*(1), 1–7. https://doi.org/10.1038/s41467-018-06168-3

Peng, Z., Vidale, J. E., Ishii, M., & Helmstetter, A. (2007). Seismicity rate immediately before and after main shock rupture from high-frequency waveforms in Japan. *Journal of Geophysical Research*, *112*(B3). https://doi.org/10.1029/2006jb004386

Peng, Z., & Zhao, P. (2009). Migration of early aftershocks following the 2004 Parkfield earthquake. *Nature Geoscience*, *2*, 877–881. https://doi.org/10.1038/ngeo697

Petrillo, G., & Lippiello, E. (2021). Testing of the foreshock hypothesis within an epidemic like description of seismicity. *Geophysical Journal International*, *225*(2), 1236–1257. https://doi.org/10.1093/gji/ggaa611

Qin, L., Ben-Zion, Y., Qiu, H., Share, P., Ross, Z., & Vernon, F. (2018). Internal structure of the San Jacinto fault zone in the trifurcation area southeast of Anza, California, from data of dense seismic arrays. *Geophysical Journal International*, *213*(1), 98–114. https://doi.org/10.1093/gji/ggx540

Ross, Z. E., & Ben-Zion, Y. (2014). Automatic picking of direct P, S seismic phases and fault zone head waves. *Geophysical Journal International*, *199*(1), 368–381. https://doi.org/10.1093/gji/ggu267

Ross, Z. E., & Cochran, E. S. (2021). Evidence for latent crustal fluid injection transients in southern California from long-duration earthquake swarms. *Geophysical Research Letters*, *48*(12), e2021GL092465. https://doi.org/10.1029/2021gl092465

Ross, Z. E., Cochran, E. S., Trugman, D. T., & Smith, J. D. (2020). 3D fault architecture controls the dynamism of earthquake swarms. *Science*, *368*(6497), 1357–1361. https://doi.org/10.1126/science.abb0779

Ross, Z. E., Trugman, D. T., Hauksson, E., & Shearer, P. M. (2019). Searching for hidden earthquakes in southern California. *Science*, *364*(6442), 767–771. https://doi.org/10.1126/science.aaw6888

Rost, S., & Thomas, C. (2002). Array seismology: Methods and applications. *Reviews of Geophysics*, *40*(3), 2–1. https://doi.org/10.1029/2000rg000100

Roux, P., Lecointre, A., Moreau, L., Campillo, M., Ben-Zion, Y., & Vernon, F. (2015). High-resolution imaging of the San Jacinto fault zone with a dense seismic array and local seismic noise. *Journal of the Acoustical Society of America*, *138*(3), 1764–1764. https://doi.org/10.1121/1.4933576

Seif, S., Zechar, J. D., Mignan, A., Nandan, S., & Wiemer, S. (2019). Foreshocks and their potential deviation from general seismicity. *Bulletin of the Seismological Society of America*, *109*(1), 1–18. https://doi.org/10.1785/0120170188

Share, P.-E., Táborík, P., Štěpančíková, P., Stemberk, J., Rockwell, T. K., Wade, A., et al. (2020). Characterizing the uppermost 100 m structure of the San Jacinto fault zone southeast of Anza, California, through joint analysis of geological, topographic, seismic and resistivity data. *Geophysical Journal International*, *222*(2), 781–794. https://doi.org/10.1093/gji/ggaa204

Shaw, J. H., Plesch, A., Tape, C., Suess, M. P., Jordan, T. H., Ely, G., et al. (2015). Unified structural representation of the southern California crust and upper mantle. *Earth and Planetary Science Letters*, *415*, 1–15. https://doi.org/10.1016/j.epsl.2015.01.016

Shearer, P. M. (2012a). Self-similar earthquake triggering, Båth's law, and foreshock/aftershock magnitudes: Simulations, theory, and results for southern California. *Journal of Geophysical Research*, *117*(B6). https://doi.org/10.1029/2011jb008957

Shearer, P. M. (2012b). Space-time clustering of seismicity in California and the distance dependence of earthquake triggering. *Journal of Geophysical Research*, *117*(B10). https://doi.org/10.1029/2012jb009471

Shelly, D. R. (2020). A high resolution seismic catalog for the initial 2019 Ridgecrest earthquake sequence: Foreshocks, aftershocks, and faulting complexity. *Seismological Research Letters*. https://doi.org/10.1785/0220190309

Sleeman, R., & Van Eck, T. (1999). Robust automatic P-phase picking: An on-line implementation in the analysis of broadband seismogram recordings. *Physics of the Earth and Planetary Interiors*, *113*(1–4), 265–275. https://doi.org/10.1016/s0031-9201(99)00007-2

Tape, C., Holtkamp, S., Silwal, V., Hawthorne, J., Kaneko, Y., Ampuero, J. P., et al. (2018). Earthquake nucleation and fault slip complexity in the lower crust of central Alaska. *Nature Geoscience*, *11*(7), 536–541. https://doi.org/10.1038/s41561-018-0144-2

Trugman, D. T., & Ross, Z. E. (2019). Pervasive foreshock activity across southern California. *Geophysical Research Letters*, *46*(15), 8772–8781. https://doi.org/10.1029/2019gl083725

van den Ende, M. P., & Ampuero, J.-P. (2020). On the statistical significance of foreshock sequences in southern California. *Geophysical Research Letters*, *47*(3), e2019GL086224. https://doi.org/10.1029/2019gl086224

Vernon, F., Ben-Zion, Y., & Hollis, D. (2014). Sage Brush Flats nodal experiment. *International Federation of Digital Seismograph Networks*. other/seismic network.

Weiss, J. (1997). The role of attenuation on acoustic emission amplitude distributions and b-values. *Bulletin of the Seismological Society of America*, *87*(5), 1362–1367.

Wyss, M., & Brune, J. N. (1967). The Alaska earthquake of 28 March 1964: A complex multiple rupture. *Bulletin of the Seismological Society of America*, *57*(5), 1017–1023. https://doi.org/10.1785/bssa0570051017

Yoon, C. E., Yoshimitsu, N., Ellsworth, W. L., & Beroza, G. C. (2019). Foreshocks and mainshock nucleation of the 1999 Mw 7.1 Hector Mine, California, earthquake. *Journal of Geophysical Research: Solid Earth*, *124*(2), 1569–1582. https://doi.org/10.1029/2018jb016383

Zhang, X., Arrowsmith, S., Tsongas, S., Hayward, C., Meng, H., & Ben-Zion, Y. (2022). A data-driven framework for automated detection of aircraft-generated signals in seismic array data using machine learning. *Seismological Society of America*, *93*(1), 226–240. https://doi.org/10.1785/0220210198

Zhu, W., & Beroza, G. C. (2019). Phasenet: A deep-neural-network-based seismic arrival-time picking method. *Geophysical Journal International*, *216*(1), 261–273.

Zigone, D., Ben-Zion, Y., Campillo, M., & Roux, P. (2015). Seismic tomography of the southern California plate boundary region from noise-based Rayleigh and Love waves. *Pure and Applied Geophysics*, *172*(5), 1007–1032. https://doi.org/10.1007/s00024-014-0872-1